Journal of Marine Science and Technology

Volume 22 | Issue 3 Article 11

NUMERICAL MODELING OF WAVE-INDUCED ROTATIONS OF A BOTTOM-HINGED FLAPPER WITH A SPH MODEL

Da-Wei Chen
Department of Harbor & River Engineering, National Taiwan Ocean University, Keelung, Taiwan, R.O.C

Shiaw-Yih Tzang
Department of Harbor & River Engineering, National Taiwan Ocean University, Keelung, Taiwan, R.O.C, sytzang@ntou.edu.tw

Chih-Min Hsieh
Department of Maritime Information and Technology, National Kaohsiung Marine University, Kaohsiung, Taiwan, R.O.C.

Yi-Chih Chow
Department of Systems Engineering and Naval Architecture, National Taiwan Ocean University, Keelung, Taiwan, R.O.C.

Jiahn-Horng Chen
Department of Systems Engineering and Naval Architecture, National Taiwan Ocean University, Keelung, Taiwan, R.O.C.

See next page for additional authors

NUMERICAL MODELING OF WAVE-INDUCED ROTATIONS OF A BOTTOM-HINGED FLAPPER WITH A SPH MODEL

Acknowledgements

This study was financially supported by National Science Council of Taiwan under grant numbers NSC-098-3114-E019-001, NSC-100-3113-E-019-001 and NSC-101-3113-E019-002.

Authors

Da-Wei Chen, Shiaw-Yih Tzang, Chih-Min Hsieh, Yi-Chih Chow, Jiahn-Horng Chen, Chen-Chou Lin, and Robert Rong-Jiann Hwang

Journal of Marine Science and Technology, Vol. 22, No. 3, pp. 372-380 (2014)
DOI: 10.6119/JMST-012-1221-1

NUMERICAL MODELING OF WAVE-INDUCED ROTATIONS OF A BOTTOM-HINGED FLAPPER WITH A SPH MODEL

Da-Wei Chen[1], Shiaw-Yih Tzang[1], Chih-Min Hsieh[2], Yi-Chih Chow[3], Jiahn-Horng Chen[3], Chen-Chou Lin[4], and Robert Rong-Jiann Hwang[3, 5]

Key words: SPH, wave, flapper, rotating angle.

ABSTRACT

In this study, a Smoothed Particle Hydrodynamics model for simulating wave-induced rotations of a bottom-hinged flapper was established in a 2-D numerical wave flume. The simulated rotating angles illustrated that the flapper could swing back and forth following harmonic wave loadings. The simulations were also seen to be in good agreement with experimental data, confirming the applicability of the present numerical model. The simulated hydrodynamic behaviors at different phases showed that the flapper moved downstream under the wave crest and upstream under the wave trough following the elliptical form of water particle trajectory. The energy conversions of a flapper during an average wave cycle showed that larger rotating angle ranges could result in higher energy conversions. However, smaller rotating angle ranges could result in higher captured efficiency.

I. INTRODUCTION

Facing the global climate change and oil crisis, issues of renewable energy have gained more and more attentions worldwide. Among the several marine renewable energies, the extraction of wave energy has been mentioned since late 18th century, but so far many technical challenges still need to be overcome. According to the World Energy Council [28], the global wave power resources in deep water (i.e. 100 m or deeper) are estimated to be 8,000~80,000 TWh/yr, with as high as 2,000 TWh/yr to be economically exploitable. In Taiwan, it was reported that the relatively larger incident wave power is in the northeastern coastal waters with estimated averaged quantity of about 10~15 kW/m, especially in winter seasons [13]. Since these coastal areas have long been protected by seawalls or even submerged detached breakwaters from larger waves, the bottom-hinged flap-type wave energy converter was chosen to extract wave energy while reducing incoming waves.

Currently, developments of the bottom-hinged flap-type convertors have reached the stage with only a few test prototypes [28]. However studies on the complex physical mechanism of interactions between wave and flapper are still insufficient. To model such a complicated mechanism could have posted great numerical challenges due to difficulties in obtaining wave forces at boundaries and setup of complex grids. Neither, setting up a regular grid system for irregular or complex geometry has ever been an easy task [15]. The regular grid system usually requires additional complex mathematical transformation that can be even more expensive than solving the problem itself. Among the few options, the smoothed particle hydrodynamics (SPH) model of the Lagrangian method is adopted in this study for its merits to easily calculate interactions between the moving objects and instant external wave forces [21].

SPH scheme is a mesh-free method for Lagrangian approach. Every particle can be easily calculated independently, especially for fast moving objects with any shape. This method is originally developed for astrophysics [7, 16]. Later, Monaghan first applied it to surface flows [17], including simulations of the dam breaking and the wave breaking. So far, SPH has become more widely applied to computational fluid mechanics such as two-phase flows [20], weakly incompressible flows [22, 23], gravity flows [18], porous flows [24, 29], and so on. Recently, the SPHysics model [11] has been developed by a group of researchers to offer open-source codes for more researchers to apply it to carry out case studies on coastal engineering, such as simulations of the green water

Paper submitted 08/20/12; revised 11/13/12; accepted 12/21/12. Author for correspondence: Shiaw-Yih Tzang (e-mail: sytzang@ntou.edu.tw).
[1] *Department of Harbor & River Engineering, National Taiwan Ocean University, Keelung, Taiwan, R.O.C.*
[2] *Department of Maritime Information and Technology, National Kaohsiung Marine University, Kaohsiung, Taiwan, R.O.C.*
[3] *Department of Systems Engineering & Naval Architecture, National Taiwan Ocean University, Keelung, Taiwan, R.O.C.*
[4] *Department of Mechanical & Mechatronic Engineering, National Taiwan Ocean University, Keelung, Taiwan, R.O.C.*
[5] *Institute of Physics, Academia Sinica, Taipei, Taiwan, R.O.C.*

overtopping [8] and the wave overtopping over typical coastal structures [6].

Moreover, for interactions between waves and solids, Monaghan *et al*. simulated physical features of the impact and entry of a rigid body traveling down a slope into water [21]. Rogers *et al*. simulated the movement of a caisson breakwater in the surf zone with a Riemann solver-based formulation [25]. The friction force between the moving caisson and the bed is modeled with a transition from static to dynamic friction force. Antoci *et al*. simulated the free oscillations of an elastic plate. Both the displacement of the elastic structure subjected to the fluid pressure and the resulting fluid flow can be obtained by the SPH model [1]. Violeau *et al*. modeled floating booms and investigated the possibility of studying the behavior of an oil spill in the vicinity of a boom to depict criteria for oil leakage [27]. Based on these noteworthy applications, the present numerical scheme herein started with the modified SPHysics code [9, 10].

The objective of this work is to develop an SPH numerical model on simulating behaviors of a rotating flapper. The proposed model may contribute to accurately simulate interactions between fluid and the wave power take-off device.

II. SPH DEVELOPMENTS

For SPH, the governing equations consist of the continuity and momentum equations for a viscous impressible flow. The equations are generally presented as:

$$\frac{1}{\rho}\frac{d\rho}{dt}+\nabla\cdot\vec{u}=0 \tag{1}$$

$$\frac{d\vec{u}}{dt}=-\frac{1}{\rho}\nabla p+\upsilon\nabla^2\vec{u}+\vec{g} \tag{2}$$

where $\vec{u}$ is the particle velocity, p the pressure, $\vec{g}$ the gravitational acceleration, ρ the fluid particle density, and υ the fluid viscosity.

1. Kernel Approximation

According to the fundamental property of the Dirac delta function, the partial differential equations of continuum fluid dynamic have to be transferred into the SPH form to principally approximate any function $A(r)$ by

$$A(r)=\int_{\Omega}A(r')W(r-r',h)dr' \tag{3}$$

where h is the smoothing length or width of a kernel function $W(r - r')$. The kernel function should generally satisfy the normalization, delta function, and compactness conditions [15]. Thus, the gradient of $A(r)$ can be expressed as:

$$\langle\nabla A(r)\rangle=\int_{\Omega}[\nabla A(r')]W(r-r',h)dr' \tag{4}$$

If the support domain of $W(r)$ being inside the computational domain Ω, Eq. (4) can be written as:

$$\langle\nabla A(r)\rangle\approx-\int_{\Omega}A(r')\nabla W(r-r',h)dr' \tag{5}$$

2. Particle Approximation

For the fluid consisting of many particles in computational domain Ω, Eq. (5) can be written as:

$$\langle\nabla A(r_a)\rangle=-\sum_b\frac{m_b}{\rho_b}A(r_b)\nabla W(r-r_b,h) \tag{6}$$

Hence, the continuity and momentum equations by SPH approximation can be written as:

$$\frac{d\rho_a}{dt}=\sum_b m_b\vec{u}_{ab}\cdot\nabla_a W_{ab} \tag{7}$$

$$\frac{d\vec{u}_a}{dt}=\sum_b m_b\left[\frac{P_a}{\rho_a^2}+\frac{P_b}{\rho_b^2}+\prod_{ab}\right]\nabla_a W_{ab}+\vec{g} \tag{8}$$

where b denotes all other particles within the active kernel function radius of $2h$. $\vec{u}_{ab}$ is the velocity variation of the particle between the velocity $\vec{u}_a$ of calculated particle a and that ($\vec{u}_b$) of other particles. W_{ab} the kernel function, P the fluid pressure, and $\prod_{ab}$ an empirical approximation of the viscosity effects ([17]). According to [2], Quintic kernel is the best compromise between accuracy and the cost of computation time. Hence, this kernel function has been adopted in present model.

3. Viscosity

The artificial viscosity proposed by [19] has been adopted as being expressed as:

$$\prod_{ab}=\begin{cases}\dfrac{-\alpha\overline{c_{ab}}\mu_{ab}}{\overline{\rho_{ab}}} & \overline{\upsilon_{ab}}\,\overline{r_{ab}}<0\\ 0 & \overline{\upsilon_{ab}}\,\overline{r_{ab}}>0\end{cases} \tag{9}$$

with

$$\mu_{ab}=\frac{h\vec{u}_{ab}r_{ab}}{r_{ab}^2+\eta^2} \tag{10}$$

where the position and the velocity of particle a and b are $r_{ab} = r_a - r_b$ and $\vec{u}_{ab}=\vec{u}_a-\vec{u}_b$ respectively. The averaged sound speed is $\bar{c}_{ab}=(\bar{c}_a+\bar{c}_b)/2$, the averaged density $\bar{\rho}_{ab} = (\rho_a+\rho_b)/2$, $\eta^2=0.01h^2$, α is a experiential parameter.

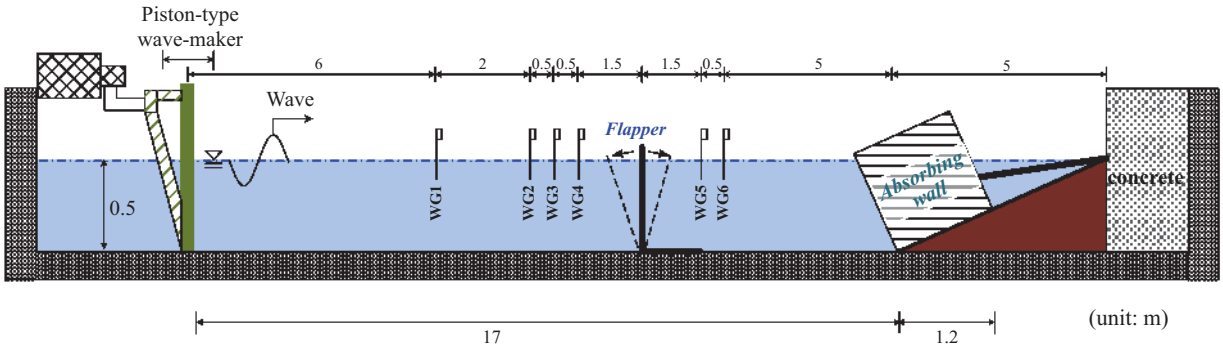

Fig. 1. Experimental setup by [14].

4. SPH Equations for a Rotating Object

According to [21], the force on each boundary particle is computed by summing up the contribution from all the surrounding water particles. Denoting the force per unit mass on a moving body boundary particle k by f_k, the equation is given by

$$f_{wp} = M\frac{dV}{dt} = \sum_k m_k f_k \tag{11}$$

where M is the mass of a rigid body, V the velocity of the center of mass, subscript wp water particles, f_{wp} the force per unit mass exerted by water particle on boundary particle. For a rotating flapper, the torque due to wave impacting on the object must be considered. In general, the wave-induced torque τ_{bp} being transferred from each boundary particle bp is given by

$$\tau_{bp} = \sum f_{wp} \times r_{H_0} \tag{12}$$

where r_{H_0} the distance from boundary particle to the hinge at H_0. Furthermore, the body force must also be considered in modeling rotating object. The equation of torque τ_{body} by body force can be written as:

$$\tau_{body} = \sum (m_{bp} \cdot g) \times r_{H_0} \tag{13}$$

where m_{bp} and $\bar{g}$ represent the mass of boundary particle b and gravity acceleration, respectively. In addition, the equation of restoring torque by a spring fixing on the hinge can be written as:

$$\tau_R = -k \cdot \theta \tag{14}$$

where k is spring constant by measuring in force per angle θ. Hence, the total torque τ_t on the rotating flapper can be written as:

$$\tau_t = \tau_{bp} + \tau_{body} + \tau_R \tag{15}$$

From the total torque τ_t, the angular acceleration $d\omega/dt$ of the rotating flapper can be found by

$$\frac{d\omega}{dt} = \frac{\tau_t}{I} \tag{16}$$

where I denotes moment of inertia.

For the rotating flapper, the rotational velocity $d\theta/dt$ being obtained by angular acceleration $d\omega/dt$ in last time step, hence, the moving angular velocity can be written as:

$$\left(\frac{d\theta}{dt}\right)^{n+1} = \left(\frac{d\theta}{dt}\right)^{n} + \left(\frac{d\omega}{dt}\right)^{n} \cdot \Delta t \tag{17}$$

where subscript "n" denotes the computational value in last time step of Δt. Thus, each boundary particle X_k in next time step can be predicted by

$$X_k^{n+1} = (X_k)_k^n + \left(\frac{d\theta}{dt}\right)^{n} \cdot \Delta t \tag{18}$$

III. MODEL SETTINGS

1. Experimental Setups

The experiments were carried out at the National Taiwan Ocean University (NTOU) [14]. The dimensions of the wave flume are 28 m in length, 0.8 m in width and 0.8 m in depth. It is equipped with a piston-type wave-maker at one end and an absorbing 1:10 sloping mattress wall at the other end, as shown in Fig. 1.

A rigid acrylic flapper with a height of 0.5 m, a width of 0.2 m and a thickness of 0.005 m was placed at the central region of the wave flume. Two torsion springs on the hinge were installed on a wood bottom to provide resorting forces, as shown in Fig. 2. The depth of the still water was 0.5 m, and the bottom-hinged flapper's freeboard was 0.2 m. In addition, free surface displacements were measured by capacity-type wave gauges (WG) located along the centerline of the flume. Four wave gauges (WG-1 to WG-4) were placed in front of the

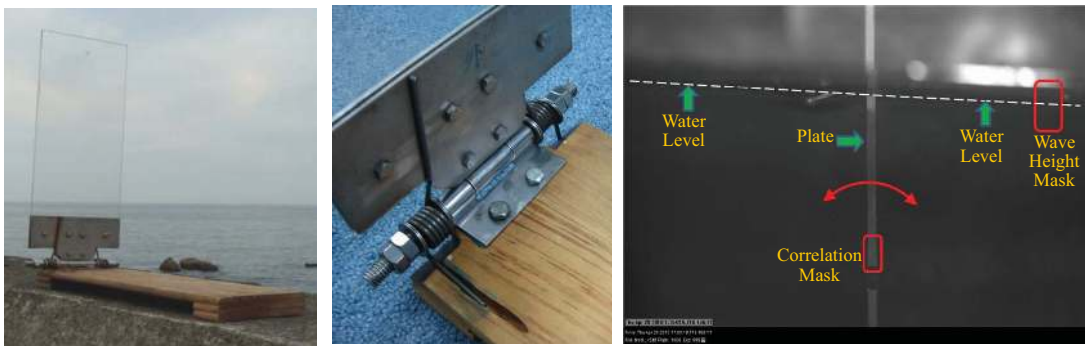

(a) Overall view (b) Torsion springs (c) Sample image

Fig. 2. The bottom-hinged flapper by [14].

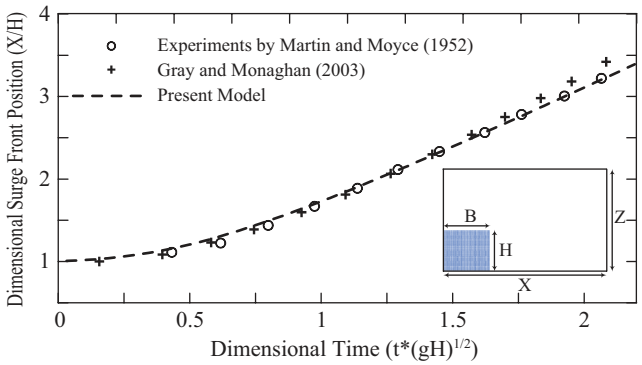

Fig. 3. Temporal surge front position for dam-breaking simulation.

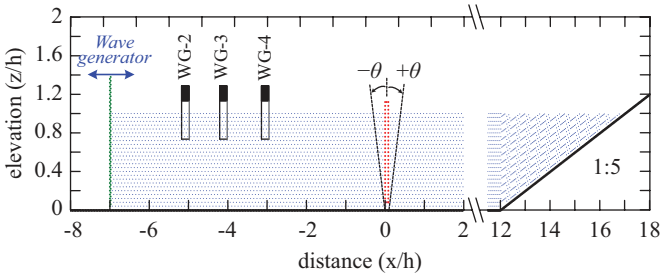

Fig. 4. Model setups and the normalized coordinates system (not to the scale).

flapper, and another two (WG-5 to WG-6) were placed between the flapper and the absorbing wall. Moreover, a high-speed camera was installed to record the angular displacement of rotating flapper in the wave flume.

To consider larger waves in northeastern coastal waters of Taiwan, experimental wave heights of 5.0~7.5 cm and wave periods of 1.34~1.56 s for a model scale of 1:20 have been applied. For more details the readers can refer to [14].

2. Computational Parameters

The 2-D SPH model for a rotating object was validated on dam-break cases and preliminarily studied on wave-flap structure interactions by [4] and [3]. In Fig. 3, it is clearly seen that the simulations by present model are quite close to those by the SPH model of [12] and experimental data on the temporal front surge positions for a dam-breaking case. Therefore, the present model is validated to be able to reasonably simulate dynamic fluid behaviors. By considering high computational efficiency and high resolutions in simulation, the previously adopted 2-D SPH numerical wave flume was slightly shortened with a length of 13 m and a depth of 0.5 m. A piston-type wave-maker was set on the upstream and a 1:5 slope on the downstream boundary for reducing reflected waves. The simulations adopted a particle spacing of $dx = dz = 0.02$ m, the empirical coefficient $\alpha = 0.03$ for viscosity term and the density of flapper of 1.18 g/cm^3. We applied the dynamic boundary conditions reported in [5] to the present study. Moreover, the initial settings of the model assigned 3129 particles on the solid boundary, 60 particles on the rotating flapper, and 13225 fluid particles. A coordinate x was normalized with respect to the water depth d of the flapper and the flapper base was set at $x/h = 0$. The wave trains propagate toward the flapper from left to right as being illustrated in Fig. 4.

3. Spring Coefficient

The spring coefficient k per rotating angle was measured by [14]. Because of pulling (flapper moving to upstream) and pushing (flapper moving to downstream) forces being given by opposite rolling springs, the restoring torques were divided into two group of experimental data, as shown in Fig. 5. The comparisons of the restoring torques with rotating angles of a flapper illustrated that the testing angles have reached 60 degrees with linear variations of rotating angles of a flapper. Hence, the simulated restoring forces in the present model could be used by linear regression analysis from experimental data, including the equations of pulling (y^-) and pushing (y^+) forces. The resulting spring coefficients k of pulling and pushing were found to be 6.701 and 6.553, respectively.

IV. MODEL VALIDATIONS

1. Surface Displacement

In order to avoid the initial unstable records in experiments

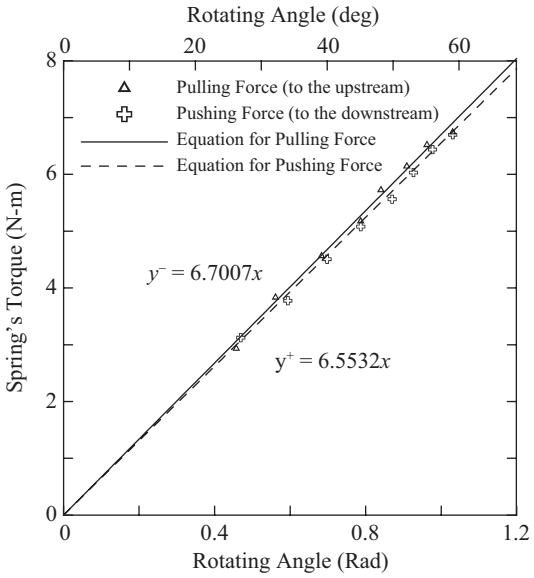

Fig. 5. The experimental data for spring torque and rotating angle.

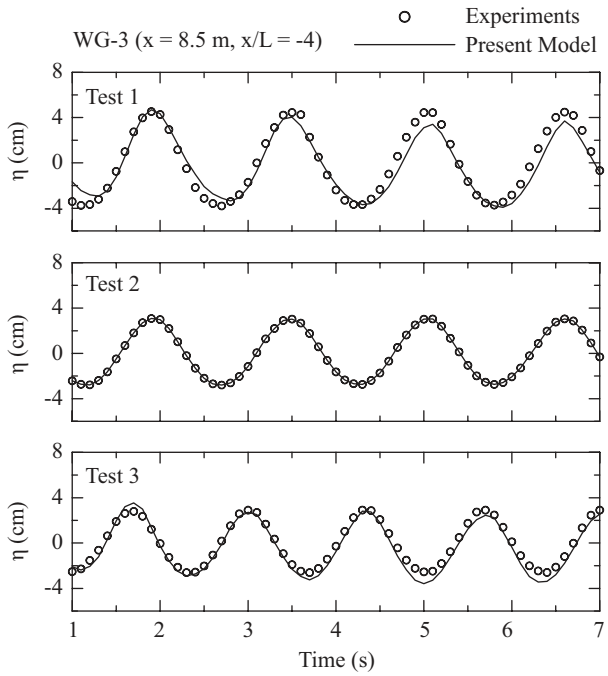

Fig. 6. Comparisons of incident waves and permeable waves around the flapper between the simulations and experimental data.

and secondary reflection in the numerical flume, the free surface displacements (η) in laboratory flume from the prescribed wave gauges (WG-2, WG-3, and WG-4) for incident waves were taken in normalized coordinate numerical flume at $x/L=-5$, $x/L=-4$, and $x/L=-3$, respectively. For accurately estimating the variations between experimental data and simulations, the errors were expressed with the statistics shown in Eqs. (19 to 21).

$$MAPE=\frac{1}{N}\sum_{i=1}^{n}\left|\frac{P_i-O_i}{O_i}\right|\times 100\% \tag{19}$$

$$RMSE=\sqrt{\frac{\sum_{i=1}^{N}(P_i-O_i)^2}{N}} \tag{20}$$

$$R=\frac{\sum_{i=1}^{n}\left[\left(P_i-\overline{P}\right)\left(O_i-\overline{O}\right)\right]}{\sqrt{\sum_{i=1}^{n}\left(P_i-\overline{P}\right)^2\sum_{i=1}^{n}\left(O_i-\overline{O}\right)^2}} \tag{21}$$

where *MAPE* is the mean absolute percentage error, *RMSE* the root mean square error, *R* the correlation coefficient, *N* the number of samples, O_i the experimental data at *i*th time step, P_i predicted value at *i*th time step by the present model, $\overline{O}$ the mean value of observations, $\overline{P}$ the value simulated at the same time.

The surface displacements were derived by searching the closest and the highest particles near the wave gauges within a radius of 2*dx*. Fig. 6 shows the time series of surface displacements from WG-3 in front of the flapper. The results included a simulation time of 6 s with approximately 4 to 5 waves in the time series. It is clear from Fig. 6 that the simulated phases of free surface displacement for different tests were in fair agreement with experimental data. Only the simulated wave crests in Test 1 and wave troughs in Test 3 were slightly smaller than experimental data. Comparisons of the values of *R*, *MAPE* and *RMSE* are presented in Table 1. We noted that the simulated surface displacements at the three wave gauges were well correlated with high correlation coefficients (0.97-0.99). The maximum percentage of error was 1.04%. The variations of *RMSE* were 0.96 to 0.54 suggesting that the simulated surface displacements by the present model agree reasonably with the experimental observations.

2. Rotating Angles of a Flapper

The rotating angles of a flapper from simulations and experimental data are shown in Fig. 7. The negative rotating angles denote counter-clockwise rotations and the positive ones clockwise rotations. The simulations show that the rotating angles of the flapper were still in good agreement with the experimental data with high correlation coefficient (*R*) of 0.96-0.99. The variations of *RMSE* were 0.82 to 1.67. In particular, the slight different wave conditions could cause the variations of the rotating angles at the high peak.

Comparisons of the rotating angles with the maximum value ($\theta_{Max.}$) and minimum value ($\theta_{Min.}$) and their sums ($\theta_{Min.}+\theta_{Max.}$) during a wave cycle for three tests are presented in Table 2. The average rotating angles had slight variations between 0.2 to 3.5 degrees. The results show that the rotating angles in experiments were slightly larger than those in simulations

Table 1. The wave conditions and validation statistics.

Gauge	Test	$H_{Exp.}$	$T_{Exp.}$	$H_{Sim.}$	$T_{Sim.}$	R	MAPE	RMSE
		(cm)	(s)	(cm)	(s)		(%)	
2	1	7.71	1.56	7.57	1.58	0.97	0.44	0.96
	2	5.36	1.56	5.52	1.57	0.98	0.54	0.64
	3	4.83	1.34	6.73	1.34	0.98	1.04	0.86
3	1	8.21	1.56	7.70	1.58	0.97	0.06	0.76
	2	5.81	1.56	5.32	1.57	0.99	0.70	0.54
	3	5.47	1.34	6.17	1.34	0.99	0.03	0.55
4	1	8.18	1.56	7.51	1.58	0.97	0.49	0.84
	2	5.63	1.56	5.37	1.57	0.96	0.09	0.59
	3	4.77	1.34	6.09	1.35	0.97	0.62	0.56

Table 2. The average maximum and minimum rotating angles of flapper and associated statistics.

Test	Exp.		Sim.		R	RMSE	∑exp.	∑sim.	MAPE
	$\theta_{Min.}$	$\theta_{Max.}$	$\theta_{Min.}$	$\theta_{Max.}$			$\theta_{Max.} + \theta_{Min.}$	$\theta_{Max.} + \theta_{Min.}$	(%)
1	-8.3	10.2	-7.9	7.6	0.98	1.67	18.5	15.5	16.22
2	-6.2	6.9	-6.0	5.9	0.99	0.82	13.1	11.9	9.16
3	-4.9	5.5	-4.9	5.6	0.96	1.11	10.4	9.9	4.81

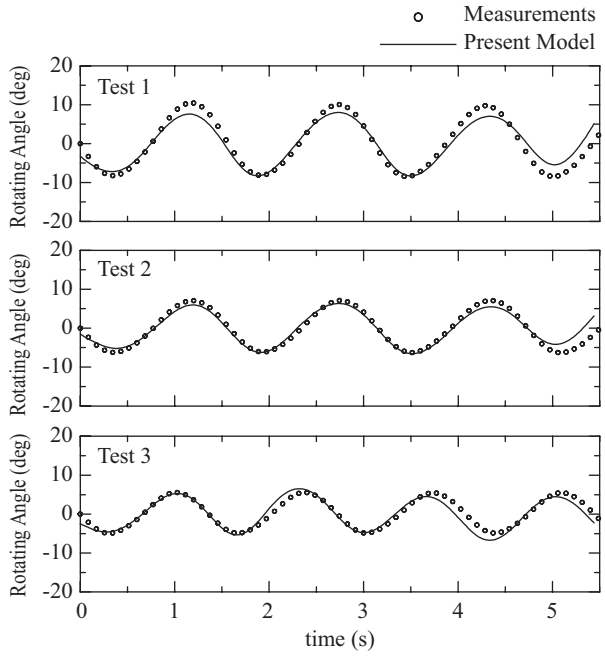

Fig. 7. Comparisons of the rotating angles of a flapper between the numerical results and the experiments.

under smaller wave conditions but were still in good agreements. The sums of average rotating angle differences from 16.22% in Test 1 to 4.81% in Test 3 between simulations and measurements for a period mainly occurring in the vicinity of wave crest. In general, the present model was still thought to be able to reasonably simulate rotations of a flapper.

V. HYDRODYNAMIC PERFORMANCE

For analyzing the kinematic property of the flapper under waves, in Test 1 wave conditions (H = 7.51 cm, T = 1.58 s) were adopted for simulation. The resulting flapper's motions and the fluid kinematic behaviors in the vicinity of the flapper were investigated, respectively.

1. Velocity Fields

The wave-induced flow fields near around a flapper are closely related to the designs of the WEC (Wave Energy Converter), especially on improving the efficiency and stability. First we divided the motion of a flapper into four phases, i.e., t/T = 0 (wave crest), 1/4, 2/4 (wave trough), and 3/4. Fig. 8 demonstrates the original SPH simulated particle form on the left panels and the post-processing velocity fields on the right panels. It is seen in Fig. 8 that as wave crest at t/T = 0 or wave trough at t/T = 2/4 approaches the flapper, the horizontal velocities reached maximum values of about 0.1 m/s under the wave crest and wave through and decayed from free-surface to the bottom, especially near the flapper at x/h = -0.4 to 0.4. When the flapper moving to the maximum angles (about ±8°), the fluid velocities of about 0.03 m/s in z-direction were nearly the same as those in x-direction at t/T = 1/4 and t/T = 3/4, as shown in Fig. 8(b) and (d).

Generally, velocities in the same direction could drive flapper back and forth, but those in opposite directions could cause the flapper in momentary stop and then to an opposite rotating direction. Note that the fluid vectors near the flapper to the bottom at the downstream and to the surface at the upstream when the flapper had maximum angles, as shown in

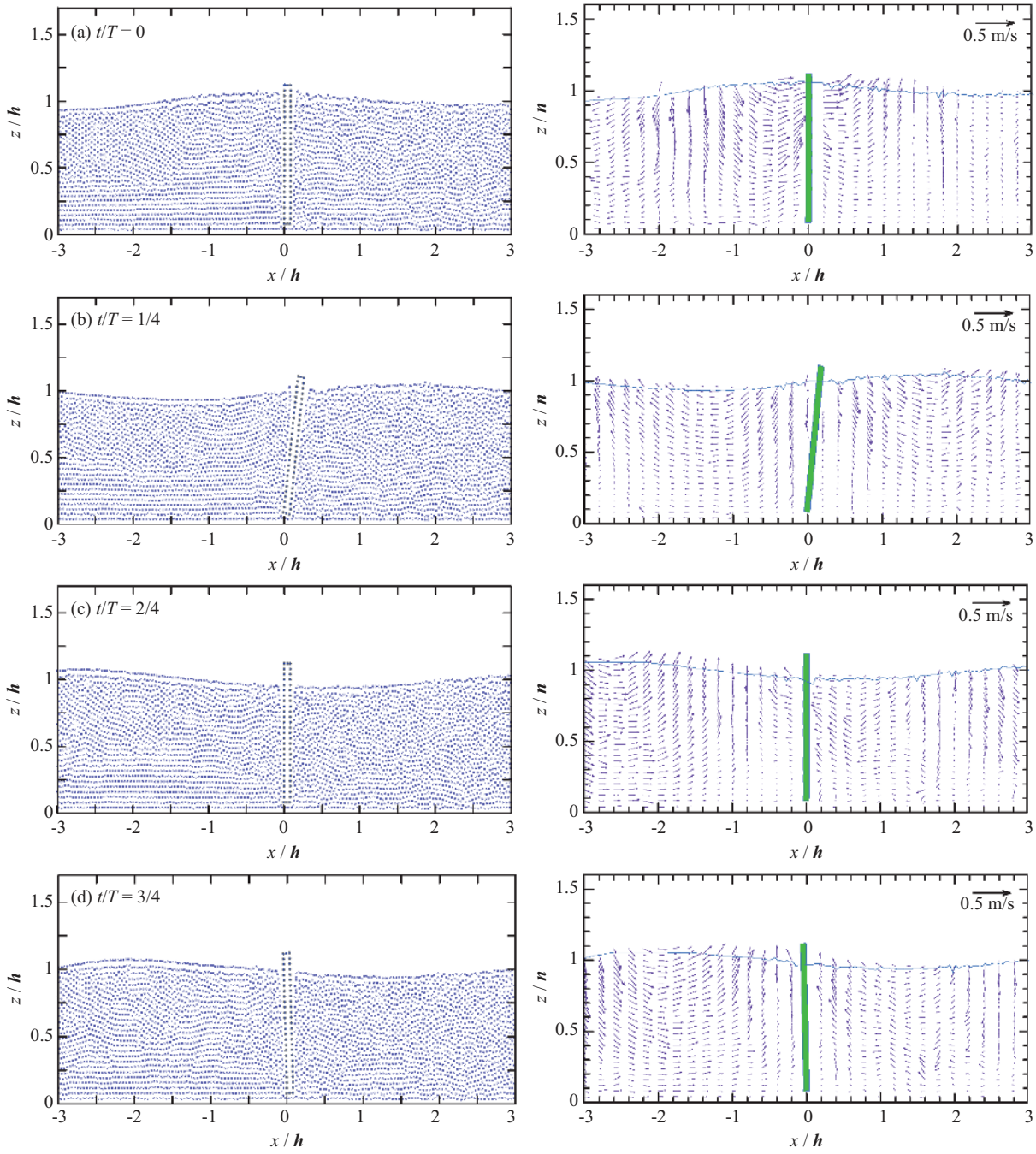

Fig. 8. The motions of a bottomed-hinged flapper at different phases. (a) *t/T* = 0; (b) *t/T* = 1/4; (c) *t/T* = 2/4; (d) *t/T* = 3/4.

Fig. 8(b) and (d). The results imply that elliptical form of water particle trajectory had quite influenced the rotations of a flapper in a whole wave cycle.

2. Motions and Power

Fig. 9 illustrates the angular motions of a rotating flapper during an averaged rotating cycle. In this figure, the positive and negative rotating angles were denoted as downstream and upstream motions of the flapper. Accordingly, wave-induced positive angular velocities to the downstream resulted in positive torques, while negative angular velocities to the upstream resulted in negative torques.

In Fig. 9, the wave-induced maximum rotating angles range between 7.88 and -8.01 degrees at about *t/T* = 1/4 and 3/4, respectively. The angular velocities at *t/T* = 0 or 1 were about 31 deg/s to the downstream and those at *t/T* = 0.54 were about -31.05 deg/s to the upstream. In particular, the average instantaneous angular velocities from *t/T* = 2/4 to 3/4 increased more rapidly, implying the flapper experiences larger angular acceleration from downstream to upstream.

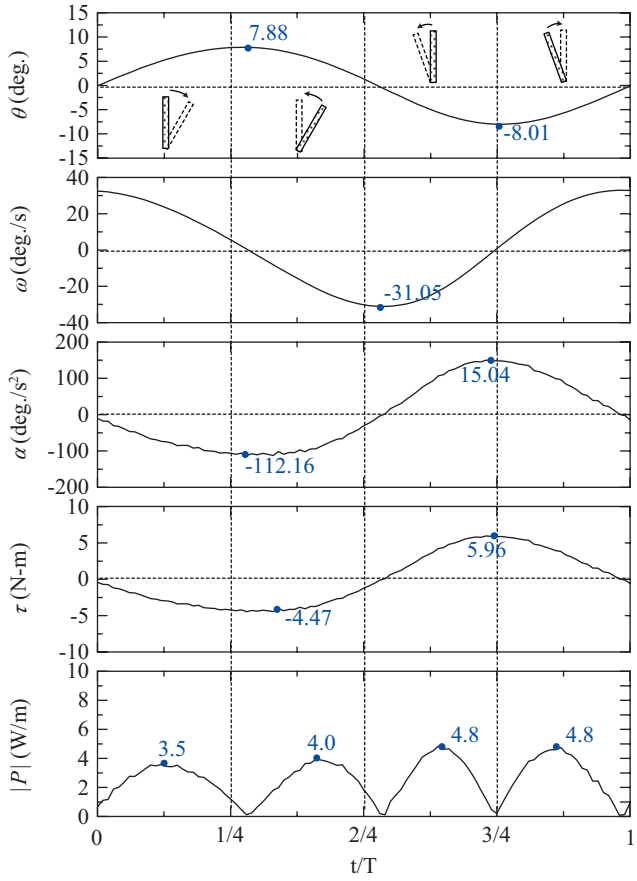

Fig. 9. Comparisons of the physical behaviors during an averaged motion of a flapper.

Obviously, the flapper's rotating velocity to upstream is faster than that to downstream. Therefore, it is clear that when the flapper being vertical to the bottom ($\theta = 0$) the angular velocities have reached the largest values without the angular acceleration. On the contrary, when the flapper being at the maximum angles the angular acceleration have reached the largest values.

In order to further understand the power capture of a flapper during an average wave cycle, the instantaneous power $|P|$ during a wave cycle could be estimated by the expression as

$$|P| = \lim_{\Delta t \to 0} \frac{\Delta W}{\Delta t} = \frac{dW}{dt} \tag{22}$$

where ΔW is the amount of the work and Δt is a period of time. Hence, the instantaneous power is the limiting value of the average power as the time interval Δt approaches zero. For averaged captured power ($|P_r|$) of a flapper, Eq. (22) can be re-written as:

$$|P_r| = \frac{1}{T}\int_0^T \tau(t)\omega(t)dt \tag{23}$$

Table 3. The wave power, wave-induced rotating angles of a flapper, and captured power.

Case	H(cm)	T(s)	θ (deg)	$\lvert P_w \rvert$ (W/m)	$\lvert P_r \rvert$ (W/m)	$\lvert P_r \rvert / \lvert P_w \rvert$ (%)
1	7.41	1.58	18.54	4.3	2.4	55.8
2	5.11	1.58	15.60	2.1	1.2	59.6
3	5.05	1.35	14.18	1.7	1.1	65.1
4	2.59	1.36	13.16	0.5	0.3	72.3
5	5.12	1.12	14.11	1.5	1.0	66.1

* $|P_w|$ is the wave power, θ is the rotating angles, $|P_r|$ is the captured power.

where τ denotes the instantaneous torque by SPH calculation, ω the instantaneous angular velocity, and T the wave period or rotating period of a flapper. Hence, the derived four instantaneous output powers in an average wave cycle is shown in the bottom panel. Because of the simple harmonic motion the zero instantaneous powers have occurred at the zero angular velocities with the maximum angular accelerations or the zero angular accelerations with the maximum angular velocities. Moreover, both of the instantaneous maximum powers under the wave crest were more than 3.5 W/m and those under the wave trough were more than 4.7 W/m. It is also noted that the larger instantaneous powers under the wave trough could be induced by the larger instantaneous angular accelerations. According to the incident wave power by $|P_w| = 0.5\, H^2 T$, in Test 1 the wave conditions could reach the average wave power of about 4.3 W/m during a wave cycle. Hence, the captured average instantaneous power of about 2.4 W/m during a wave cycle suggested about 55.8% of efficiency of the flapper.

3. Energy Conversion

According to [26], wave characteristics nearby Port of Keelung in winter of 2008 could be adopted as the typical input waves for evaluating the WEC conversion of a flapper. Comparisons of the related wave conditions, wave power, wave-induced rotation of a flapper, and the captured power are shown in Table 3. It is clearly seen that larger wave power by $|P_w| = 0.5\, H^2 T$ with larger wave heights or periods could cause larger rotating angles of a flapper, resulting in higher captured power by flapper's motions. The wave powers from 0.5 W/m to 4.3 W/m could cause the flapper's average rotating angles to be 13.16° to 18.54°. The energy conversions from 0.3 W/m to 2.4 W/m suggested the converted efficiency of about 72.3% to 55.8%.

Note that a flapper with larger rotating angles could generate higher powers but with lower efficiency of captured wave power. On the other hand, a flapper with smaller rotating angles could generate higher efficiencies of power conversion. As a result, with similar wave periods (i.e., case 1 & 2, and case 3 & 4), the waves with higher wave heights could cause larger rotating angles and higher converted energy. With

similar wave heights (i.e., case 2 & 3 & 5), waves with longer wave periods were also seen to generate higher converted energy.

VI. CONCLUSIONS

A SPH 2-D numerical wave flume model was adopted to simulate wave-induced rotations of a bottom-hinged flapper with a restoring spring system. The simulated angular motions were noted to be in reasonable agreement with experimental measurements for an acrylic flapper.

By comparing the simulations with experimental data, we found that the surface displacements and simulated rotating angles of a flapper were highly correlated and had low error variations. Hence, the flapper could reasonable swing back and forth following harmonic wave loadings using the present model. Simulations of the hydrodynamic behaviors at different phases point out that the flapper moved to downstream under the wave crest and upstream under the wave trough. We also noted that the flapper rotated with the elliptical trajectory of water particles.

The simulated energy conversions of a flapper during an average wave cycle suggest that the larger range of the wave-inducd flapper's rotating angles could generate the higher converted energy. On the other hand, the smaller range of rotating angle could generate higher captured power efficiency. For similar wave periods, higher waves could induce larger rotating angle ranges and higher energy conversions. For similar wave heights, waves with longer wave periods could generate higher converted energy.

ACKNOWLEDGMENTS

This study was financially supported by National Science Council of Taiwan under grant numbers NSC-098-3114-E-019-001, NSC-100-3113-E-019-001 and NSC-101-3113-E-019-002.

REFERENCES

1. Antoci, C., Gallati, M., and Sibilla, S., "Numerical simulation of fluid-structure interaction by SPH," *4th MIT Conference on Computational Fluid and Solid Mechanics*, pp. 879-890 (2007).
2. Capone, T., Panizzo, A., Cecioni, C., and Darlymple, R. A., "Accuracy and stability of numerical schemes in SPH," *Second International Workshop*, pp. 156-160 (2007).
3. Chen, D.-W., Tzang, S.-Y., Hsieh, C.-M., Chen, J.-H., Zeng, N.-Y., and Hwang, R.-R., "Numerical simulation of hydrodynamic behavior on wave-flap structure interactions with a SPH model," *Proceedings of the Conference on Asian and Pacific Coasts (APAC2011)*, pp. 1378-1385 (2011).
4. Chen, D.-W., Tzang, S.-Y., Hsieh, C.-M., Zeng, N.-Y., and Hwang, R.-R., "Numerical study on typhoon wave-induced damages on a breakwater," *The 6th International Conference on Coastal Structures (Coastal Structures 2011)*, pp. C3-085 (2011).
5. Crespo, A. J. C., Gomez-Gesteira, M., and Dalrymple, R. A., "Boundary conditions generated by dynamic particles in SPH methods," *CMC-Computers Materials & Continua*, Vol. 5, No. 3, pp. 173-184 (2007).
6. Didier, E. and Neves, M. G., "Wave overtopping of a typical coastal structure of the Portuguese coast using a SPH model," *Journal of Coastal Research*, Special Issue No. 56, pp. 496-500 (2009).
7. Gingold, R. A. and Monaghan, J. J., "Smoothed particle hydrodynamics - Theory and application to non-spherical stars," *Monthly Notices of the Royal Astronomical Society*, Vol. 181, pp. 375-389 (1977).
8. Gomez-Gesteira, M., Cerqueiro, D., Crespo, C., and Dalrymple, R. A., "Green water overtopping analyzed with a SPH model," *Ocean Engineering*, Vol. 32, No. 2, pp. 223-238 (2005).
9. Gomez-Gesteira, M., Crespo, A. J. C., Rogers, B. D., Dalrymple, R. A., Dominguez, J. M., and Barreiro, A., "SPHysics – development of a free-surface fluid solver – Part 2: Efficiency and test cases," *Computers & Geosciences*, Vol. 48, pp. 300-307 (2012).
10. Gomez-Gesteira, M., Rogers, B. D., Crespo, A. J. C., Dalrymple, R. A., Narayanaswamy, M., and Dominguez, J. M., "SPHysics – development of a free-surface fluid solver – Part 1: Theory and formulations," *Computers & Geosciences*, Vol. 48, pp. 289-299 (2012).
11. Gomez-Gesteira, M., Rogers, B. D., Dalrymple, R. A., and Crespo, A. J. C., "State-of-the-art of classical SPH for free-surface flows," *Journal of Hydraulic Research*, Vol. 48, Extra Issue, pp. 6-27 (2010).
12. Gray, J. P. and Monaghan, J. J., "Caldera collapse and the generation of waves," *Geochemistry, Geophysics, Geosystems*, Vol. 4, p. 28 (2003).
13. Hsu, B. H. and Yan, Z. W., "Introduction to the perspectives of marine energy developments," *Physical Bimonthly*, Vol. 29, No. 3, pp. 718-726 (2007).
14. Lee, Y.-H., Wang, D.-L., Chang, Y.-C., Chow, Y.-C., and Lin, C.-C., "Preliminary experimental investigation on the kinematic characteristics of flap-type wave energy converter," *Proceedings of the 32rd Ocean Engineering Conference in Taiwan*, pp. 837-842 (2010).
15. Liu, G. R. and Liu, M. B., *Smoothed Particle Hydrodynamics: A Meshfree Particle Method*, World Scientific (2003).
16. Lucy, L. B., "Numerical approach to the testing of the fission hypothesis," *Astronomical Journal*, Vol. 82, No. 12, pp. 1013-1024 (1977).
17. Monaghan, J. J., "Simulating free surface flows with SPH," *Journal of Computational Physics*, Vol. 110, No. 2, pp. 399-406 (1994).
18. Monaghan, J. J., "Simulating gravity currents with SPH lock gates," *Mathematics Reports and Preprints*, Vol. 95/5 (1995).
19. Monaghan, J. J., "Smoothed particle hydrodynamics," *Annual Review of Astronomy and Astrophysics*, Vol. 30, No. 1, pp. 543-574 (1992).
20. Monaghan, J. J. and Kocharyan, A., "SPH simulation of multi-phase flow," *Computer Physics Communications*, Vol. 87, Nos. 1-2, pp. 225-235 (1995).
21. Monaghan, J. J., Kos, A., and Issa, N., "Fluid motion generated by impact," *Journal of Waterway Port Coastal and Ocean Engineering-Asce*, Vol. 129, No. 6, pp. 250-259 (2003).
22. Morris, J., "Modeling low Reynolds number incompressible flows using SPH," *Journal of Computational Physics*, Vol. 136, No. 1, pp. 214-226 (1997).
23. Morris, J. P. and Monaghan, J. J., "A switch to reduce SPH viscosity," *Journal of Computational Physics*, Vol. 136, No. 1, pp. 41-50 (1997).
24. Morris, J. P., Zhu, Y., and Fox, P. J., "Parallel simulations of pore-scale flow through porous media," *Computers and Geotechnics*, Vol. 25, No. 4, pp. 227-246 (1999).
25. Rogers, B. D., Dalrymple, R. A., and Stansby, P. K., "Simulation of caisson breakwater movement using 2-D SPH," *Journal of Hydraulic Research*, Vol. 48, pp. 135-141 (2010).
26. Tzang, S.-Y., Chen, J.-H., Yang, J.-Z., and Wang, C.-C., "The analysis on wave power poten-tials on the northeast coastal waters of Taiwan," *Proceedings of the 11th International Conference on Fluid Control, Measurements and Visualization (FLUCOME 2011)*, Paper No. 196 (2011).
27. Violeau, D., Buvat, C., Abed-Meraim, K., and de Nanteuil, E., "Numerical modelling of boom and oil spill with SPH," *Coastal Engineering*, Vol. 54, No. 12, pp. 895-913 (2007).
28. WEC, *Survey of Energy Resources (2010)*, World Energy Council (2010).
29. Zhu, Y., Fox, P. J., and Morris, J. P., "A pore-scale numerical model for flow through porous media," *International Journal for Numerical and Analytical Methods in Geomechanics*, Vol. 23, No. 9, pp. 881-904 (1999).